Journal of Water Process Engineering 63 (2024) 105477

Contents lists available at ScienceDirect

Journal of Water Process Engineering

journal homepage: www.elsevier.com/locate/jwpe

# Selective reactive oxygen and nitrogen species production in plasma-activated water via dielectric barrier discharge reactor: An innovative method for tuning and its impact on dye degradation

Saeed Kooshki *, Pankaj Pareek, Mario Janda, Zdenko Machala *

*Faculty of Mathematics, Physics, and Informatics, Comenius University Bratislava, Slovakia*

ARTICLE INFO

Editor: Gamze Varank

*Keywords:*
Plasma-activated water
Selective reactive oxygen and nitrogen species production
Cost estimation
Wastewater treatment
Non-thermal plasma

ABSTRACT

Water treated by non-thermal gas plasma shows a great potential across various applications, e.g. in wastewater cleaning, agriculture, and bio-medicine. Maximizing the plasma water treatment efficacy requires precise control over reactive oxygen/nitrogen species (RONS) concentrations. This study emphasizes the importance of tuning the plasma system for selective production of RONS in water, for both higher operational efficacy and better economic efficiency in dye wastewater treatment. We propose an innovative approach for tuning RONS. In particular, ceramic electrode (Ce) and higher reactor temperatures result in a higher hydrogen peroxide ($H_2O_2$) production in PAW, up to 16 mg.l$^{-1}$ within 30 min, and minimal nitrite production. Conversely, copper electrode with water-cooling system (Cuw) result in higher nitrite concentrations, up to 80 mg.l$^{-1}$ within the same treatment time, but negligible $H_2O_2$ production. Selective RONS production significantly affects methylene blue dye degradation. Ce setup yields an efficient dye degradation (1.04 g.kWh$^{-1}$), while Cuw setup proves inefficient and synthesizes additional by-products in water by nitration mechanism. Finally, a total cost estimation analysis showed that potentially scaled-up plasma technology operates at low energy costs if compared with advanced oxidation processes. Selective RONS production for the dye degradation can lead to almost 30 % reduction in the total costs.

## 1. Introduction

Generation of non-thermal plasma (NTP) in atmospheric air leads to the production of various reactive oxygen and nitrogen species (RONS) due to the presence of nitrogen, oxygen, and moisture in the atmosphere. In direct NTP-water interaction, the RONS diffuse into the water, ultimately resulting in the production of plasma-activated water (PAW) [1–3]. The PAW technology is one of the fastest growing new technologies due to its continuously developing applications in medicine, agriculture, wastewater treatment, food science and technology, etc. [4]. The RONS in PAW mostly include long-lived species, such as nitrates ($NO_3^-$), nitrites ($NO_2^-$), hydrogen peroxide ($H_2O_2$), and ozone ($O_3$), with typical lifetimes of days, hours and minutes, and short-lived ones, such as hydroxyl radicals ($OH^\bullet$), nitric oxide ($NO^\bullet$), superoxide ($O_2^-$), peroxynitrate ($OONO_2^-$), and peroxynitrite ($ONOO^-$) with sub-second lifetimes. The RONS in PAW induce significant physicochemical changes in water properties. Each of these species plays a specific role in different PAW applications [5]. Therefore, it is crucial to develop effective techniques for fine-tuning the RONS composition in PAW to optimize its efficiency across a wide range of applications.

Different RONS have different significance in various applications. Reactive oxygen species (ROS), such as $H_2O_2$, $O_3$, $OH^\bullet$, and $ONOO^-$ play a key role in microbial inactivation, selective killing of cancer cells, and enhancing the shelf life of various food products such as fruits, vegetables, etc. [6–9]. Reactive nitrogen species (RNS), such as $NO_3^-$ and $NO_2^-$ can be used as sources of nitrogen for replacement of synthetic nitrogen fertilizers in numerous agriculture applications [10–12]. The simultaneous generation of both ROS and RNS in plasma discharges makes it challenging to assess the individual impact of each species. Some species exhibit beneficial properties for their intended application, while others may have adverse effects [13]. For example, ROS play important roles in advanced oxidation processes (AOPs) for wastewater treatment [14–16], while RNS are not necessary for this purpose and may potentially reduce the effectiveness of PAW in such processes. Therefore, tailoring the production of ROS and RNS for different applications of PAW is crucial for a targeted and successful implementation of plasma

* Corresponding authors.
*E-mail addresses:* SaeedKoushki@gmail.com (S. Kooshki), machala@fmph.uniba.sk (Z. Machala).

https://doi.org/10.1016/j.jwpe.2024.105477
Received 4 March 2024; Received in revised form 3 May 2024; Accepted 11 May 2024
Available online 16 May 2024
2214-7144/© 2024 The Authors. Published by Elsevier Ltd. This is an open access article under the CC BY-NC-ND license (http://creativecommons.org/licenses/by-nc-nd/4.0/).

technology [17,18].

Pervious research studies have explored methods to control RONS production, such as the use of various shielding gases around the plasma jet [19,20], or employing hybrid electrolytic systems within different gas environments [21]. Some reports have focused on the different chemistry induced by different plasma discharges, highlighting, for example, that streamer corona strongly contributes to the formation of ROS, while the more energetic transient spark or glow discharge allow to manipulate the ratio of ROS vs. RNS [22–26]. Among various NTP systems, the Dielectric Barrier Discharge (DBD) stands out as one of the prominent plasma sources for PAW generation due to its simplicity in construction and control [27–29]. Ganesh et al. [30] reported a special DBD reactor using helical electrode with very low specific energy consumption for selective RNS production. Pandey et al. [31] also reported a surface DBD reactor with the selective generation of nitrate and nitrite and zero concentration of hydrogen peroxide in the PAW. However, a cost-effective and high-performance approach for the selective production of ROS and RNS is still an area that requires further exploration.

Recently, we developed a fountain dielectric barrier discharge (FDBD) reactor [32] with a design similar to that of Kovačević et al. [33]. In this study, we use different central electrode materials and a water-cooling system in the FDBD reactor to produce a PAW with selective and controllable generation of RONS. This approach represents a simpler and more cost-effective alternative to conventional methods for controlling and tuning the ratio of ROS and RNS. In addition, our study demonstrates the significant impact of controlling ROS and RNS production in the tested PAW on its application for wastewater treatment, particularly in model dye degradation. We show that increasing the concentration of ROS in PAW can notably enhance the degradation yield of methylene blue. Conversely, increasing the ratio of RNS leads to the formation of nitrated species, resulting in a lower degradation efficiency and conversion of methylene blue molecules into another by-product, such as malachite green. These results are consistent with those reported by Wang et al. [34], who indicated that the formation of nitrogenous species is the primary factor contributing to the low organic dye degradation efficiency in air plasma, while the concentrations of oxidizing species played the major role in the dye decomposition. The total cost estimation for our reactor plasma-based water treatment indicates that the selective production of RONS for dye degradation can result in a significant reduction in the total cost, estimated to be up to 30 %.

## 2. Methods and materials

### 2.1. Plasma setups

Fig. 1 depicts the schematic diagram of the experimental setup comprising the FDBD reactor with a changeable outer electrode and central tube, a high voltage AC transformer (15 kV, 20 kHz), a water pump and water tank for recirculating PAW in the system, and a DC power supply (24 V) for the water pumps. The reactor is suitable for the treatment of large volumes of water, recirculating it through the plasma region at relatively high flow rates of up to 2 $l.min^{-1}$. The reactor is designed with a coaxial cylindrical shape, where a quartz tube with dimensions of 200 × 30 mm and a thickness of 1.5 mm serves as the dielectric, and the gap distance is approximately 4 mm. Water is pumped into the reactor and then falls from the top of the central tube onto its outer surface, passing in laminar flow through the microdischarge region. As such, the design of the reactor utilizes water as the central electrode, and it is possible to substitute the central electrode even with a non-conductive material.

In order to assess the influence of the central tube material on the concentrations of RONS within the generated PAW, we conducted experiments employing two types of central tubes: copper (Cu) and alumina ceramic (Ce). It is worth noting that the material of the central tube interacts with the plasma zone and the treated water, which can impact chemical reactions occurring in the PAW. As another modification of the setup with respect to our previous study [32], we incorporated a water-cooling system as an outer electrode in the FDBD reactor to examine the effects of total reactor temperature on the concentrations of RONS. The overall temperature of the reactor with the water-cooling system was kept at 20 ± 2 °C during the experiments. The water-cooling system not only affects the overall temperature of the reactor but also significantly influences the electrical characteristics of the discharge. We categorize the results into four distinct cases in the FDBD plasma reactor:

(1) system without the water cooling using the copper central tube (Cu setup),
(2) system without the water cooling using the ceramic central tube (Ce setup),
(3) system with the water cooling using the copper central tube (Cuw setup),

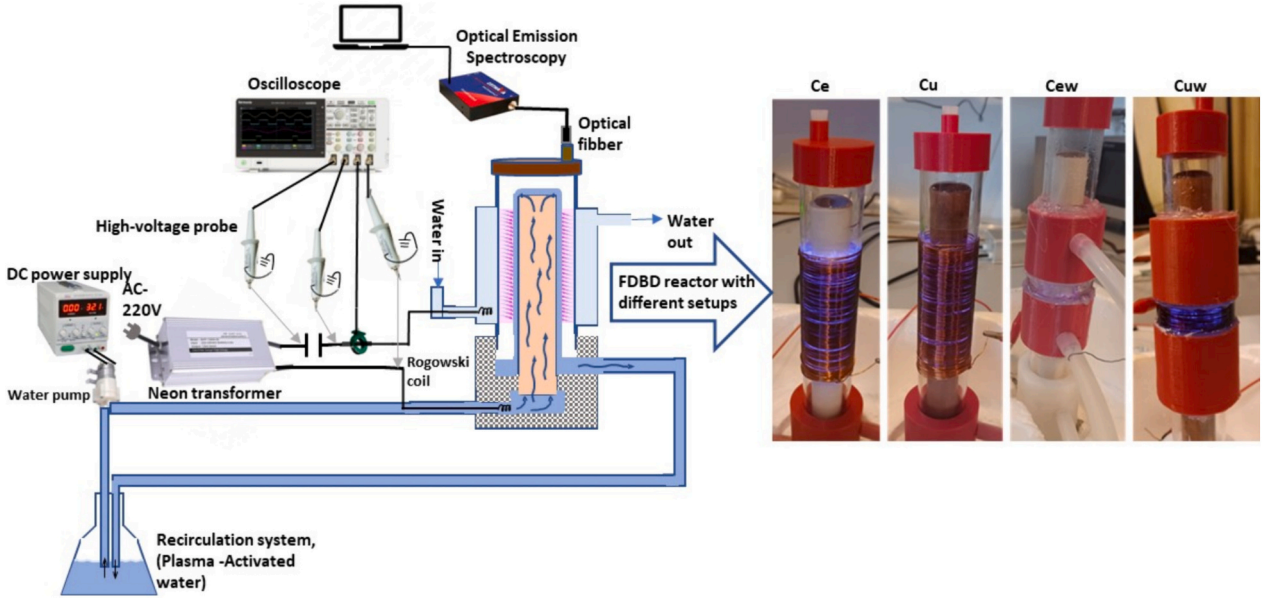


**Fig. 1.** Sheme of the FDBD reactor system and photos of the 4 different setups.

(4) system with the water cooling using the ceramic central tube (Cew setup).

By systematically investigating these 4 cases, we aim to elucidate the impact of the central tube material and the presence of the water-cooling system on the concentrations of RONS. All experiments were conducted using a 220 V input voltage of the neon transformer providing up to 15 kV peak-to-peak AC voltage with the typical frequency 20 kHz. The two key parameters for PAW generation were the plasma treatment time and the recirculating water flow rate in the reactor. In order to ensure the consistency of the measurements, all experiments are conducted three times. The results, depicted in the respective graphs, include associated instrumental errors along with statistical error bars represented as standard deviations.

### 2.2. Physical discharge characterization

For measuring the gas temperature in the discharge and analysing the gaseous reactive species in the plasma zone of the FDBD reactor, we employed Optical Emission Spectroscopy (OES) using Ocean Optics SD 2000 spectrometer. This two-channel spectrometer operates within a wavelength range of 200–1000 nm and offers a spectral resolution of 0.6 nm in the wavelength range of 200–500 nm and a spectral resolution of 1.2 nm in the spectral range of 500–1100 nm. The plasma emission was collected from the top of the reactor with the vertical line of sight integrating emission signals of multiple FDBD microdischarges over the length of the central tube.

The voltage and current waveforms were measured by the digital oscilloscope (TBS2104, Tektronix) with tree high voltage probes (P6015A, Tektronix), and a current monitor (Rogowski coil Person Electronics, model 2877). The input power was measured by the method of Lissajous figures. The area enclosed by the Lissajous voltage-charge curve represents the energy dissipated by the discharge per period. The transported charges in the discharge were indirectly determined through a 560 pF circuit equivalent capacitor in series with the reactor, by differential voltage measurement using two high-voltage probes from both sides of the capacitor (since none of the sides is grounded). The operating frequency was 19 ± 1 kHz.

### 2.3. Chemical analysis of PAW

To monitor the pH, oxidation-reduction potential (ORP), and temperature of each PAW sample, a portable pH/ORP meter (WTW 3110, Weilheim, Germany) with temperature probe was used continuously. The electrical conductivity (EC) of the PAW samples was measured using a Digital Conductivity Meter GMH 3430.

The concentrations of $H_2O_2$, $NO_3^-$, and $NO_2^-$ in treated water were measured by the colorimetric assays and absorption spectroscopy using the UV–vis spectrophotometer (Shimadzu UV-1800). The concentration of $H_2O_2$ is determined by measuring the intensity of a yellow-colored complex formed when titanium oxosulphate reagent reacts with $H_2O_2$ in an acidic medium, and the UV–vis absorption is measured at a wavelength of 407 nm [35]. $NO_2^-$ is quantified from the intensity of an azo dye formed when $NO_2^-$ react with *N*-(1-naphthyl)-ethylenediamine dihydrochloride in phosphoric acid solution (Griess reagent), measured at 540 nm. [22]. The total $NO_X^-$ concentration was determined using a reagent mixture of 10 mM 2,6-xylenol and acids ($H_2SO_4$ : $H_3PO_4$ in a 1:1 ratio) with the absorption maximum recorded between 290 nm and 350 nm. The maximum peak intensity is directly proportional to the concentration of $NO_X^-$. Finally, the $NO_3^-$ concentration was obtained by subtracting the $NO_2^-$ concentration (measured by Griess) from the total $NO_X^-$ concentration. A control sample was prepared using de-ionized water following the same procedure.

### 2.4. Methylene blue (MB) degradation

The MB concentration was measured using UV–Vis absorption spectroscopic technique. The percentage of decolourization and degradation rate was calculated from the Eq. (1):

$$\text{Degradation rate } [\%] = \frac{A_0 - A}{A_0} \times 100 \tag{1}$$

where, $A_0$ symbolizes the initial absorbance, and A represents the absorbance of the dye after the treatment. The absorption is measured in ultraviolet region with the peaks around 292 nm.

The dye degradation efficiency was measured using energy yield calculations and is defined as the ratio between the amount of dye removed during the plasma treatment and the consumed energy. The energy yield (Y) for the contaminant removal process was calculated using Eq. (2),

$$Y(g/kWh) = \left[ V(l) \times C_0\left(g.l^{-1}\right) \times \left( \text{degradation rate\%} \times \frac{1}{100} \right) \right] \Big/ \left[ P(kW) \times t(h) \right] \tag{2}$$

where V, $C_0$, P, and t are the solution volume, initial concentration of the dye sample, the applied power, and the degradation time, respectively [34]. In this study we take the MB solution with an initial concentration of 10 $mg.l^{-1}$.

## 3. Result and discussion

### 3.1. Physical discharge characterization

To validate the performance of the reactor, we recorded the waveforms of the voltage and the current across the reactor. The voltage-current waveforms of air discharge with water created by the FDBD Reactor with (Cu), (Ce), (Cuw), and (Cew) systems are shown in Fig. 2 (a), (b), (c), and (d), respectively. It is evident that the applied voltage provided by the neon sign transformer closely resembles a standard sinusoidal waveform. However, the current waveform displays several high-amplitude pulses. The observed discharge current characteristics of all the plasma setups showed the combination of several micro-discharges, which show that the generated air plasma was a filamentary DBD micro-discharge in nature. In the water-cooling systems (Cuw and Cew), the voltage amplitudes are higher and these current pulses typically exhibit minimal amplitude, and the occurrence of micro-discharges is relatively low. However, the breakdown voltage peaks in the (Cuw) and (Cew) setups (Fig. 2(c) and (d)) were higher compared to (Ce) and (Cu) (Fig. 2(b) and (a)).

In general, the total current in Ce and Cu setups comprises a combination of the dielectric capacitive current and the discharge current. However, in the case of Cuw and Cew setups, the total current is a combination of the water outer electrode current, dielectric capacitive current, and the discharge current. It showed the larger discharge-current peaks in the FDBD reactor without water cooling system (Ce and Cu) compared to with water cooling setups (Cew and Cuw) in both the positive and negative half-cycles. Higher temperatures in Ce and Cu setups without water cooling could improve the capacitive characteristics of the reactor and increase the charge accumulated on the dielectric surface in each cycle of the applied voltage. Hence, a higher temperature of the reactor lead to a higher capacitance, a higher space charge is accumulated on the quartz tube surface [36,37]. Therefore, at the peak of positive and negative half-cycle, rapid discharge of accumulated charges occurs, which is shown as intense filamentary peaks in the case of (Ce) and (Cu) discharge-current waveforms (Fig. 2(a), (b)).

However, in the cases of Cuw and Cew setups with water cooling (Fig. 2(c), (d)), the maximum applied voltage is higher, resulting in a greater discharge power compared to Ce and Cu setups. Fig. 2(e) depicts

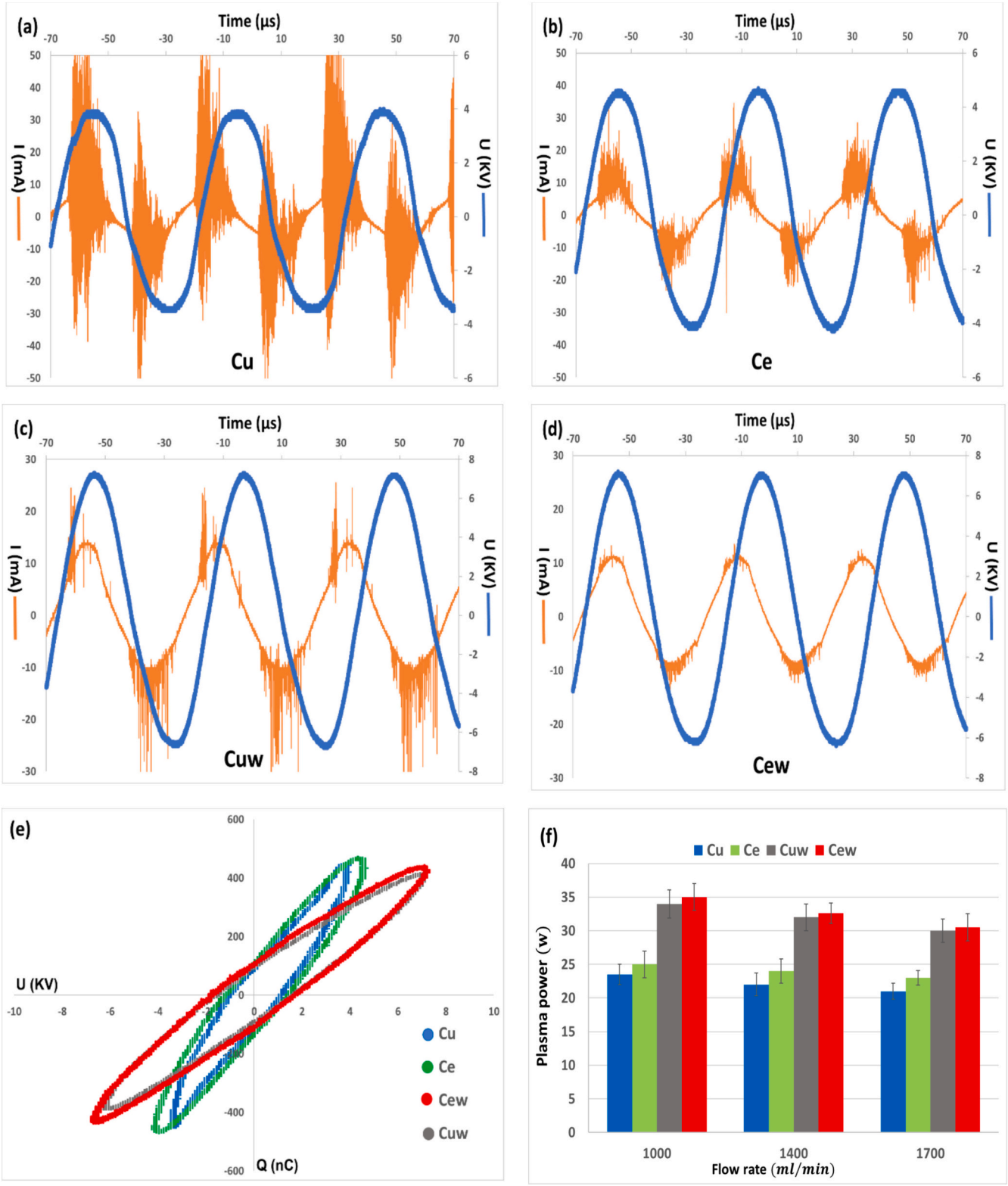


**Fig. 2.** Electrical characterization and Voltage-Current waveform in the FDBD reactor at different setups at PAW flow rate 1400 ml.min$^{-1}$, (a) copper tube (Cu), (b) ceramic tube (Ce), (c) copper tube with water cooling system (Cuw), and (d) ceramic tube with water cooling system (Cew). (e) Lissajous curve for different setups (Cu, Ce, Cuw, and Cew), (f) plasma power consumption for different setups at different PAW flow rate.

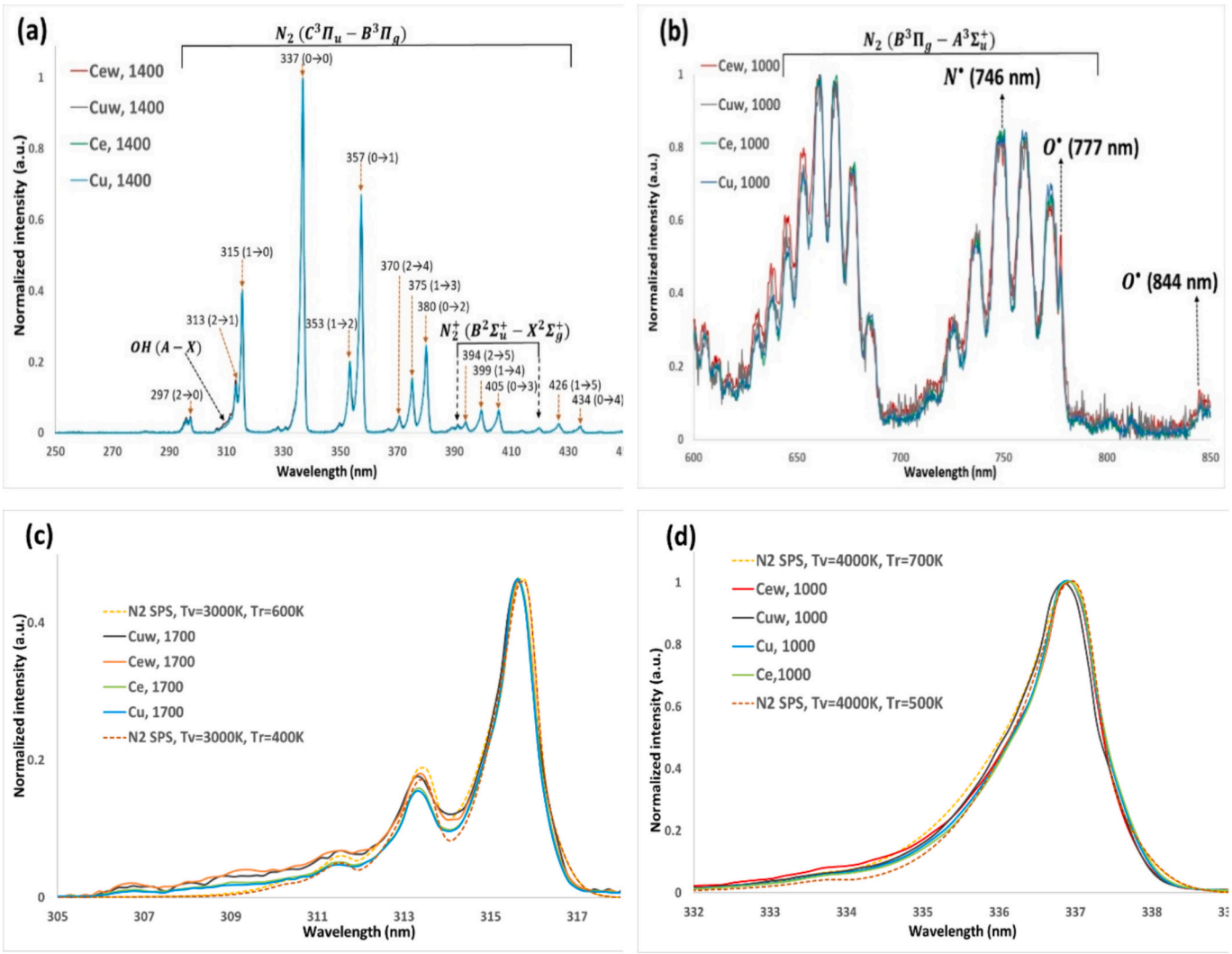


**Fig. 3.** The optical emission spectrum (OES) of air plasma provided from different setups of the FDBD. (a) $N_2\left(C^3\Pi_u - B^3\Pi_g\right)$ and $N_2^+\left(B^2\Sigma_u^+ - X^2\Sigma_g^+\right)$ in UV range, (b) $N_2\left(B^3\Pi_g - A^3\Sigma_u^+\right)$ in the vis-NIR range, (c) multiple $N_2$ SPS bands fitted to estimate vibrational temperature *at different setups with flow rate 1400* ml.min$^{-1}$, (d) a high intensity emission of $N_2$ SPS 0–0 vibrational band fitted with the simulated spectrum to estimate rotational temperature at different setups with flow rate 1000 ml.min$^{-1}$.

the comparison of transported charge-voltage Lissajous curves for different setups. The total area of the Lissajous curves and plasma power consumption vary across different reactor setups, following the pattern: Cuw > Cew > Ce > Cu (Fig. 2 (f)). Observations indicate that higher flow rates are associated with lower reactor temperatures and a slight reduction in overall plasma power consumption.

Fig. 3 presents the typical optical emission spectrum (OES) generated by the discharge in the FDBD reactor. The OES encompasses emissions from various systems, namely $N_2$ second positive system (SPS) $\left(N_2\left(C^3\Pi_u - B^3\Pi_g\right)\right)$, $N_2^+$ first negative system (FNS) $\left(N_2^+\left(B^2\Sigma_u^+ - X^2\Sigma_g^+\right)\right)$, and $N_2$ first positive system (FPS) $\left(N_2\left(B^3\Pi_g - A^3\Sigma_u^+\right)\right)$.

The OES in the discharge regime is predominantly characterized by strong emission bands from the SPS within the 250–450 nm range marked in Fig. 3(a). In addition, we observed some week intensity emission bands of $N_2^+$ FNS with a peak at 391.4 nm. Furthermore, a faint emission band attributed to hydroxyl radicals $OH\left(A^2\Sigma - X^2\Pi\right)$ appears at around 309 nm. The emission bands of hydroxyl radicals are possibly generated through elastic collisions involving high-energy electrons and $H_2O$ molecules. In gas-liquid discharge (air-water), water vapor from the liquid surface can directly enter the discharge region due to the heating effect of the discharge. The presence of water vapor enhances the consumption of high-energy electrons and quenches the excited $N_2$ by $H_2O$ molecules [38]. Moreover, Fig. 3(b) shows that there are two atomic oxygen spectral lines at 777 nm and 844.6 nm [39,40].

The vibrational temperature ($T_v$) and rotational temperature ($T_r$) of different discharge setups at varying flow rates are estimated by fitting the experimental $N_2$ SPS spectra with simulated ones. Spectral simulation was performed using Specair software [41]. Fig. 3(c), and (d) depict the best experimental spectra for each setup and flow rate, fitted with the corresponding simulated spectra. The vibrational temperature ranges from 3000 to 4000 K, while the rotational temperature falls within 400–700 K. Consistent with plasma power consumption, the setups with water cooling systems (Cuw and Cew) exhibit slightly higher vibrational and rotational temperatures compared to the setups without water cooling (Cu and Ce). It is noteworthy to emphasize that the determined rotational temperature does not signify the overall average gas temperature in the reactor.

### 3.1.1. *Physical properties of PAW*

Fig. 4 shows the variation of the physical properties of produced

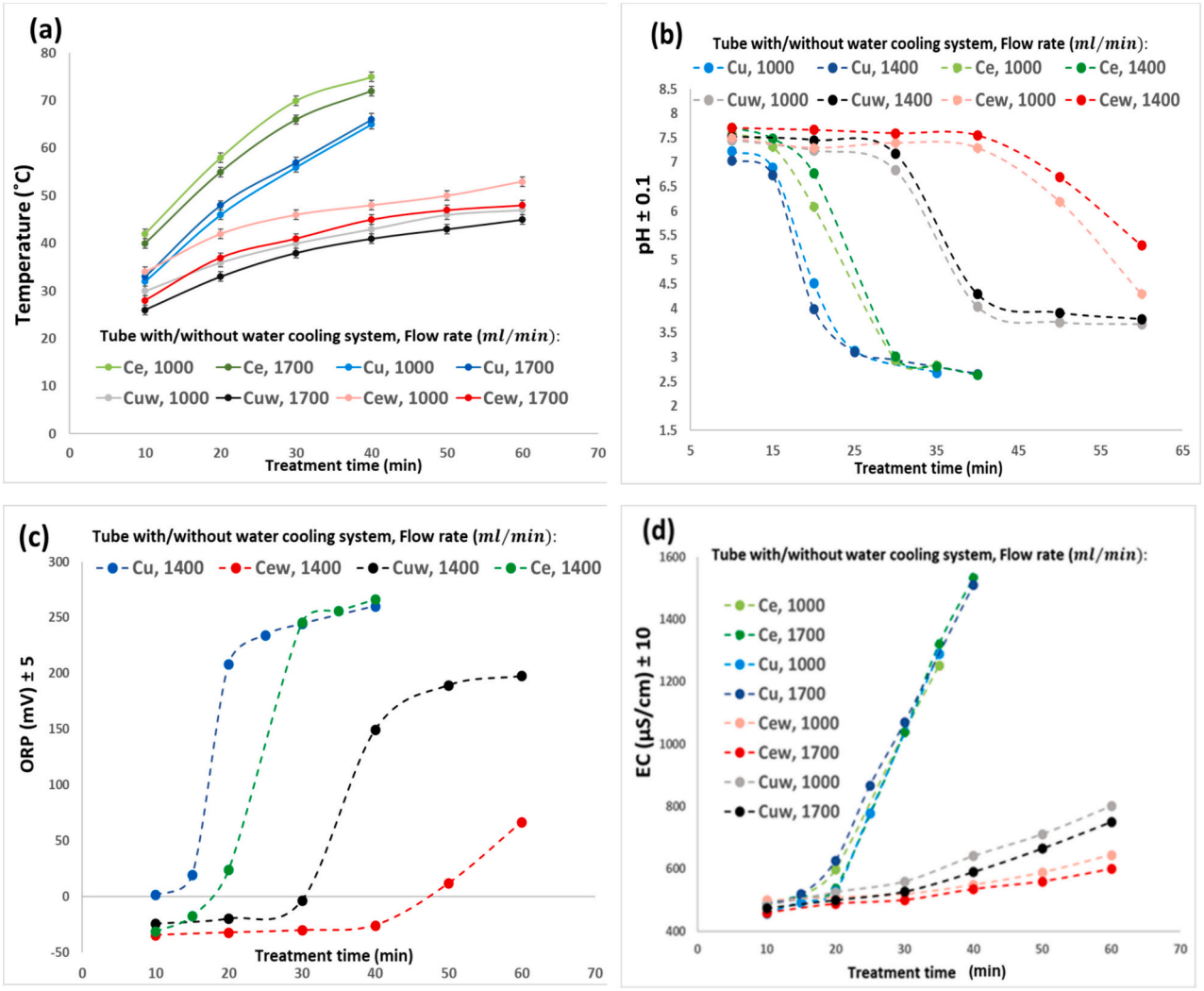


**Fig. 4.** Physical properties of generated PAW with different FDBD reactor setups versus plasma treatment time (min) at different PAW flow rate (ml.min$^{-1}$), (a) PAW temperature, (b) pH variation, (c) ORP variation, and (d) electrical conductivity variation (µS.cm$^{-1}$).

$$HNO_3(aq) \leftrightarrow NO_3^-(aq) + H^+ \quad (5)$$

$$HNO_2(aq) \leftrightarrow NO_2^-(aq) + H^+ \quad (6)$$

$$NO_2(aq) + NO_2(aq) + H_2O \leftrightarrow NO_2^-(aq) + NO_3^-(aq) + 2H^+ \quad (7)$$

$$NO(aq) + NO_2(aq) + H_2O \leftrightarrow NO_2^-(aq) + NO_2^-(aq) + 2H^+ \quad (8)$$

$$H_2O(g) + e \rightarrow H^\bullet + OH^\bullet \quad (9)$$

$$OH(g,aq) + OH(g,aq) \rightarrow H_2O_2(g,aq) \quad (10)$$

$$HO_2(aq) + e\ (aq) \rightarrow HO_2^-(aq) \quad (11)$$

$$HO_2^-(aq) + H^+ \rightarrow H_2O_2(aq) \quad (12)$$

$$O(^1D)(aq) + H_2O \rightarrow H_2O_2(aq) \quad (13)$$

$$3NO_2^-(aq) + 3H^+ \rightarrow 2NO(aq) + NO_3^-(aq) + H_3O^+ \quad (14)$$

$$NO_2^-(aq) + H_2O_2(aq) \rightarrow NO_3^-(aq) + H_2O \quad (15)$$

$$NO_2^- + H_2O_2 + H^+ \rightleftarrows ONOOH + H_2O \quad (16)$$

PAW versus plasma treatment time at different setups of the FDBD reactor. The initial temperature of water was 20 ± 2 °C. Fig. 4(a) illustrates that the temperature of produced PAW showed a rapid increase over treatment time in the case of Ce and Cu setups, whereas a slower rise was observed in the water-cooling Cew and Cuw setups. Although these results appear to conflict with the plasma temperature measurements obtained using OES in different setups, a coherent theoretical explanation exists that reconciles both observations. The plasma temperature at different setups is changed in the following order: Cew > Cuw > Ce > Cu, but it is essential to note that the temperature of the produced PAW is influenced and modified by the total gas temperature within the reactor.

The average gas temperature increase in the gap ($\Delta T_g$) is defined by the following equation [42],

$$\Delta T_g = \left(\frac{d}{\lambda}\right) \times \left(\frac{P}{F}\right) \times (1-\eta) \times a. \quad (3)$$

where, λ and d are the heat conductivity of the gas and the gap distance, respectively. The ratio (P/F) represents the relationship between power and the efficient electrode area. Considering the plasma power consumption at different setups this ratio exhibits the following order: Cuw > Cew > Cu > Ce. The coefficient d is given by 1/3 for the cooling of one surface (in cases of the Ce and Cu setups) and 1/12 for the cooling of both surfaces (in cases of the Cew and Cuw setups). The factor (1 − η) accounts for the energy not used in free radicals formation [42]. The last Eq. (3) shows that the gap temperature is a balance between power and heat dissipated by cooling the reactor. Furthermore, the total gas temperature ($T_g$) in the gap distance can be described with the following equation:

$$T_g = T_W + \Delta T_g \quad (4)$$

where, $T_W$ is the wall temperature [42]. In water cooling setups (Cew and Cuw), the wall temperature is maintained at 20 ± 2 °C. However, without the water-cooling system (Ce and Cu), the wall temperature rapidly exceeds more than 100 °C. As a result, the total gas temperature is theoretically adjusted in the following order: Ce > Cu > Cew > Cuw. Higher gas temperature leads to higher PAW temperature accordingly, which aligns with the measured PAW temperature versus plasma treatment time as shown in Fig. 4(a).

The physical characteristics of micro-discharges influence the temperature of the gas in the reactor. Fig. 2 shows that without water cooling (Cu and Ce setups), the current pulses are stronger and more frequent compared to Cuw and Cew setups, so they result in higher gas temperature which then leads to a higher water vapor production in the Ce and Cu setups compared to Cew and Cuw setups. Consequently, different gas temperature in various setups with and without water cooling must lead to different rates of water evaporation and consequently different chemical composition of the produced PAW.

The dissolved RONS in water influence the measured pH, oxidation reduction potential (ORP), and electrical conductivity (EC). The initial pH, ORP, and EC of tap water (control) was 7.6, −36 mV, and 443 μS. $cm^{-1}$, respectively. In Fig. 4(b), it is evident that when employing the FDBD reactor with Cu and Ce setups, the treated water undergoes significant acidification within 20 and 25 min, respectively. Conversely, in the Cuw and Cew setups, the pH value of the treated water exhibits a significantly slower decrease that starts after longer treatment time.

The reduction in pH of PAW can be attributed to the generation of $NO_x$, and nitrous and nitric acids during the interaction between plasma and water. These nitrogen species in water release $H^+$ ions leading to acidification, for example by the reactions (5)–(8). More significant decrease of pH thus indicates the formation of a higher concentration of acidifying species (gaseous (H)$NO_x$) observed in the Cu and Ce setups. This could be explained by stronger and more numerous micro-discharge current pulses in the Cu and Ce setups.

The higher and faster increase in ORP observed in PAW prepared by the Cu and Ce setups, compared to the Cuw and Cew setups (Fig. 4(c)), can also be attributed to the enhanced formation and solvation of oxidizing species such as OH radicals (formed in the plasma by reaction 9) due to the higher temperature and increased water evaporation. The increase in ORP and decrease in pH of water after plasma-water exposure was previously reported by many authors [3,10,43].

Gradual accumulation of $NO_2^-$ (aq) and $NO_3^-$ (aq) ions and decreasing pH (i.e. increasing concentration of $H^+$ ions) can also explain the increasing electrical conductivity of PAW, as shown on Fig. 4(d). Here again, the faster increase of EC in the Cu and Ce setups compared to the Cuw and Cew setups indicates enhanced generation of RONS in the setups without water cooling.

### 3.2. Chemical properties of PAW

High chemical reactivity of PAW can be attributed to the presence of various short-lived and long-lived (RONS). However, only the long-lived species like nitrates ($NO_3^-$), nitrites ($NO_2^-$) and hydrogen peroxide ($H_2O_2$) are stable enough to be detected in the generated PAW at the end of the plasma treatment time. Low concentrations of short-lived RONS could be detected only if they are continuously formed in PAW in post-treatment time via chemical reactions among long-lived species.

For this reason, we focus here on the detection of $NO_3^-$, $NO_2^-$ and $H_2O_2$ in the generated PAW. As was already mentioned, the formation of $NO_3^-$, $NO_2^-$ can proceed by reactions 5–8 from solvated nitrogen oxides, and nitrous and nitric acids. $H_2O_2$ is formed dominantly by electron-impact dissociation of water molecules (reaction 9) and subsequent recombination of hydroxyl radicals (reaction 10) both in gas and aqueous phase. Solvation of gaseous $H_2O_2$ to water is very fast, and can contribute significantly to accumulation of $H_2O_2$ in water [44]. Moreover, $H_2O_2$ (aq) could be also formed by liquid phase reactions from solvated short-lived $O(^1D)$, OH(aq), or $HO_2$(aq) radicals (reactions 10–13) [45–47].

In the Fig. 5, we present evolutions of $NO_3^-$, $NO_2^-$ and $H_2O_2$ concentration as function of treatment time in the PAW prepared by the different plasma setups. With increasing time and increasing energy input, more and more $NO_3^-$, $NO_2^-$ and $H_2O_2$ species are produced. On the other hand, with increasing concentration of these species, the importance of mutual chemical reactions in liquid is also growing. The rate of these reactions may differ in different setups depending on the liquid temperature or pH. Under acidic conditions, for example, a disproportionation reaction (reaction 14) converts $NO_2^-$ to $NO_3^{--}$. $NO_3^-$ can be also produced by oxidation of $NO_2^-$ by $H_2O_2$ (reaction 15).

#### 3.2.1. Hydrogen peroxide concentrations

Fig. 5 (a) illustrates the hydrogen peroxide concentrations produced in PAW at different flow rates using Cu and Ce setups. The $H_2O_2$ concentration was higher in the Ce and Cu setups compared to the Cew/Cuw setups. In the both Cew and Cuw setups, the maximum concentration of $H_2O_2$ was approximately 1 $mg.l^{-1}$, which is close to the detection limit of our analytical method. In the PAW prepared by water cooling systems (Cew/Cuw setups), the treated water inside the chamber is not heated. Therefore, less water vapor was present inside the chamber. It probably leads to lower production of hydroxyl and other radicals and thus also lower production rate of hydrogen peroxide, since reactions of OH and other radicals are the main $H_2O_2$ formation channels (reactions 10–13). Lower reactivity of plasma generated in Cuw/Cew setups could be also attributed to smaller numbers of micro-discharge current pulses and

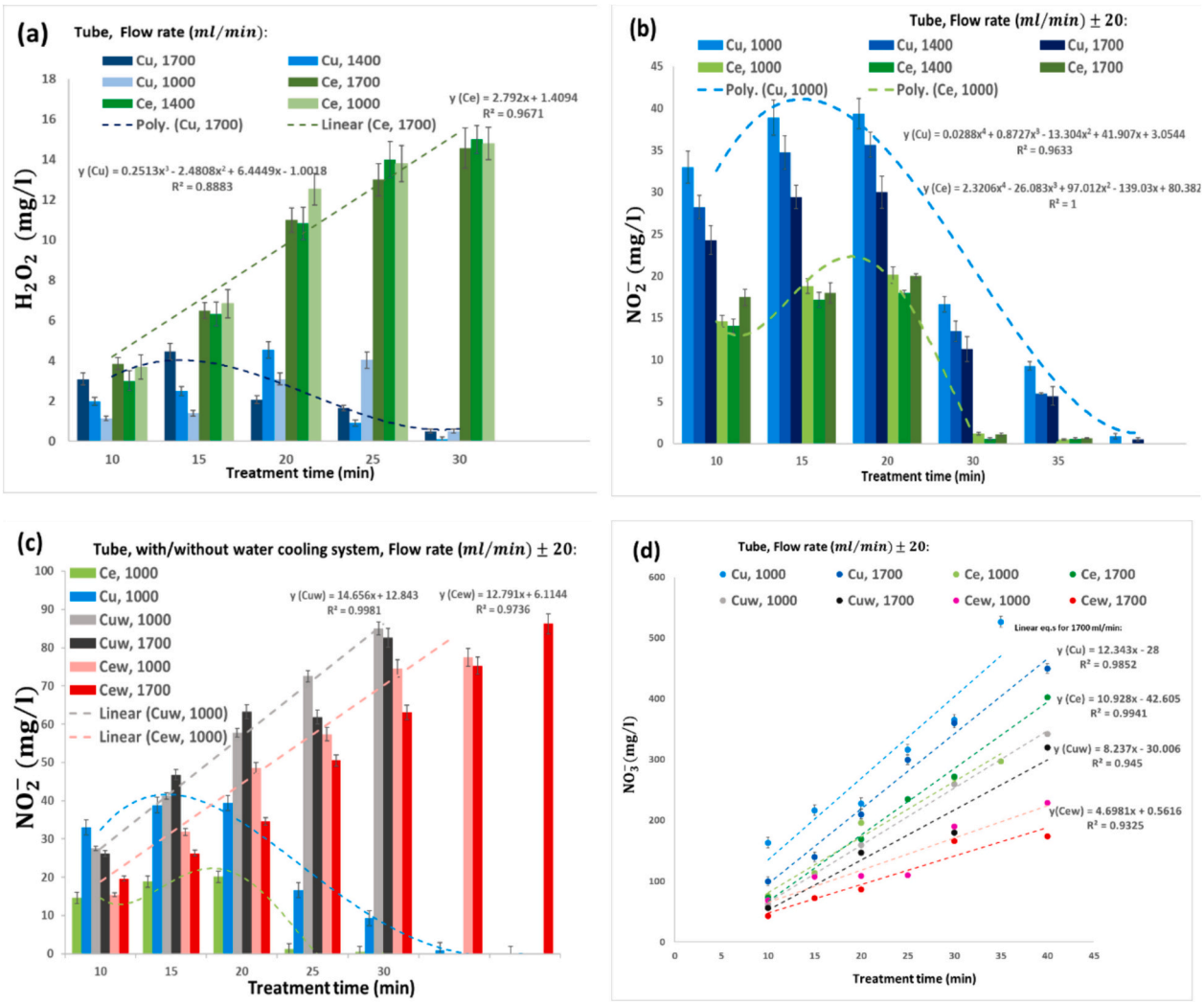


**Fig. 5.** RONS concentration versus plasma treatment time (min) at different PAW flow rate (ml.min$^{-1}$) (a) Hydrogen peroxide in the Ce and Cu setups. (b) Nitrite Concentration in the Ce and Cu setups, (c) Nitrite Concentration in the Cew and Cuw setups, and (d) Nitrate Concentration in PAW versus plasma setups.

their lower amplitudes (Fig. 2).

$H_2O_2$ concentration in PAW prepared by the Ce setup shows a linear increase with plasma treatment time, with a maximum concentration of 15 ± 1 mg.l$^{-1}$as depicted in Fig. 5 (a). The $H_2O_2$ concentration in the PAW prepared by the Cu setup exhibits a non-linear trend during the plasma treatment time, with a rise and a fall pattern and a maximum concentration of approximately 5 ± 1 mg.l$^{-1}$ achieved before declining gradually to zero with prolonged treatment. Previous studies have mainly reported a linear increase in $H_2O_2$ production with plasma treatment time in PAW production particularly when noble gases or closed systems are used [22,38,18,48]. However, some literature has also indicated a non-linear relationship between $H_2O_2$ concentration and plasma treatment time, with a slight rise and fall timeline pattern observed in air plasma discharge [49,34,25].

The production of hydrogen peroxide is dominantly influenced by water evaporation and dissociation and the formation of hydroxyl radicals (reactions 9–10), which is determined by the power dissipated in the discharge. Linear increase of $H_2O_2$ (aq) concentration in Ce setup can be explained by a relatively constant production of $H_2O_2$ precursors (mainly $OH^{\bullet}$ radicals) by plasma and a lower importance of the processes responsible for $H_2O_2$ (aq) removal in water. As the water is heated by the plasma, water vapor gradually accumulates inside the container over time. It then leads to an increased formation of $OH^{\bullet}$ radicals, resulting in higher $H_2O_2$ level in water [31,22]. The observed temperature increases in PAW during the plasma treatment time (Fig. 4 (a)) aligns with this phenomenon. PAW generated using the Ce setup, which experiences higher heating temperatures, yields higher concentrations of $H_2O_2$.

When comparing Cu and Ce setups, we must consider the fact that the composition of the central tube material may have an influence on the chemical reactions taking place in the PAW. This is because the material interacts with both the plasma zone and water, thereby affecting the overall reaction dynamics the $H_2O_2$ concentration in PAW from Cu setup first increases, later declines. This declining trend could be theoretically explained by Fenton reactions, where cuprous ions would catalyse the decomposition of $H_2O_2$ to generate hydroxyl radicals The Fenton-like reaction has the potential to take place either on the surface of the copper tube or in the liquid phase, facilitated by the presence of dissolved copper ions [50–53]. It has often been assumed that in a Fenton-like reaction, hydrogen peroxide will be scavenged by cuprous ions in a chain reaction, as described by reactions 17–20 [53,54].

$$Cu^{1+} + H_2O_2 \longrightarrow Cu^{2+} + OH^- + OH^{\bullet} \quad (17)$$

$$OH^{\bullet} + H_2O_2 \longrightarrow H_2O + O_2^{\bullet -} + H^+ \quad (18)$$

$$Cu^{2+} + O_2^{\bullet -} + H^+ + H_2O_2 \longrightarrow Cu^{1+} + O_2 + OH^{\bullet} + H_2O \quad (19)$$

$$Cu^{1+} + OH^{\bullet} + H^{+} \longrightarrow Cu^{2+} + H_2O \quad (20)$$

The rate constants of these chain reactions are pH dependent with higher rate constants at lower pH [53]. Therefore, after 20–25 min of treatment time, the reactions are accelerated following the drop in pH under acidic conditions, and copper probably acts as a catalyst to degrade $H_2O_2$ quickly. In addition, the observed evolution of $H_2O_2$ (aq) concentration in Ce and Cu setups can be also linked to the evolution of $NO_2^-$ (aq) concentration, as discussed in the following subsection.

### 3.2.2. Nitrite concentrations

Fig. 5 (b) and (c) shows the nitrite ($NO_2^-$) concentrations in the PAW generated by the FDBD reactor in the tested Ce, Cu, Cew, and Cuw setups. The $NO_2^-$(aq) concentration in the PAW prepared by Cu and Ce setups follows a non-linear rising and falling trend during the plasma treatment time, with a maximum concentration of 20 ± 1 mg.l$^{-1}$ and 38 ± 1 mg.l$^{-1}$ for the Ce and Cu setups, respectively. In both cases, the concentration of $NO_2^-$ gradually decreases to zero after 20 min of plasma treatment (Fig. 5(b)), when the pH drops and PAW becomes acidic (Fig. 4(b)).

The rise and fall pattern in $NO_2^-$ concentration is similar to the pattern in $H_2O_2$ (aq) concentration in Cu setup. It is therefore possible that the rapid reaction between $NO_2^-$ ions and $H_2O_2$ in acidic conditions, resulting in the formation of more stable $NO_3^-$ ions (reaction 15) or short-lived peroxynitrous acid or peroxynitrite anions (reaction 16), can explain the decreasing concentration of $NO_2^-$ (aq) ions [25,14]. This explanation would be thus consistent with previous studies which have suggested that up to 90 % of nitrite loss in the PAW can be attributed to excessive reactive oxygen species (such as $O_3$, $H_2O_2$, etc.) [31].

However, the concentration of $H_2O_2$ (aq) is significantly lower than the concentration of $NO_2^-$ (aq) in the Cu setup and probably cannot explain the oxidation of all $NO_2^-$ (aq) ions to $NO_3^-$ (aq) ions. Moreover, in the Ce setup, where the concentration of $NO_2^-$ (aq) and $H_2O_2$ (aq) are comparable, the observed trends are different. Hence, we assume that it is rather the disproportionation reaction of $NO_2^-$ (aq) to $NO_3^-$ (aq) (reaction 14) at acidic conditions that can better explain the decreasing $NO_2^-$ (aq) concentration after 20 min of plasma treatment. However, the reaction between $NO_2^-$ ions and $H_2O_2$ probably still plays a certain role and the influence of $H_2O_2$ can explain why the observed maximum concentration of $NO_2^-$ ions in PAW prepared using the Ce setup is lower than the $NO_2^-$ (aq) concentration in the Cu setup.

The concentration of $NO_2^-$ ions in PAW generated using the water cooling (Cew and Cuw setups) shows a linear increase with the plasma treatment time compared to the Cu and Ce setups (Fig. 5 (c)). In the Cuw and Cew setups the pH did not drop below 3.5 even after long time plasma treatment (Fig. 4(b)) and there was a negligible amount of $H_2O_2$ in PAW. These two missing $NO_2^-$- depleting factors can explain the linear increase of $NO_2^-$(aq) concentration in PAW generated using the Cew and Cuw setups.

Cuw and Cew setups produce PAW with more predominant RNS over ROS. Most probably there was some $H_2O_2$ produced but due to higher concentration of RNS it was consumed by reactions with $NO_2^-$ This observation is consistent with previous studies which have suggested that up to 90 % of nitrite loss in the PAW can be attributed to excessive reactive oxygen species (such as $O_3$, $H_2O_2$, etc.) [31].

### 3.2.3. Nitrate concentrations

Fig. 5(d) illustrates the concentration of $NO_3^-$ ions in PAW prepared using different setups: Ce, Cu, Cew, and Cuw. $NO_3^-$ ions exhibit the highest concentration among the studied reactive species in all PAW samples. This finding is consistent with previous studies that suggest the reactions between $NO_2^-$ ions and $H_2O_2$ (reaction 15) and disproportionation reaction (reaction 14) lead to the formation of stable $NO_3^-$ ions, which persist in PAW even after several weeks of plasma treatment [55,13]. The conversion of $NO_2^-$ to $NO_3^-$ continues until $NO_2^-$ nearly disappears after several weeks. This disproportionation conversion is accelerated in acidic conditions [52].

It is observed that the concentration of $NO_3^-$ ions in PAW prepared by the Cu and Ce setups is higher compared to the PAW prepared by Cuw and Cew setups. This difference can be partly attributed to the lower conversion rate of $NO_2^-$ to $NO_3^-$ in the PAW generated by the Cuw and Cew setups due to the absence of $H_2O_2$ and higher pH. Consequently, a lower concentration of $NO_3^-$ was produced in the Cuw and Cew setups. However, even if we make a sum of $NO_2^-$ and $NO_3^-$ concentrations, more $NO_x^-$ ions are produced in Cu and Ce setups compared to Cuw and Cew setups. This indicates more efficient plasma chemistry in the Ce and Cu systems due to stronger and more numerous microdischarge current

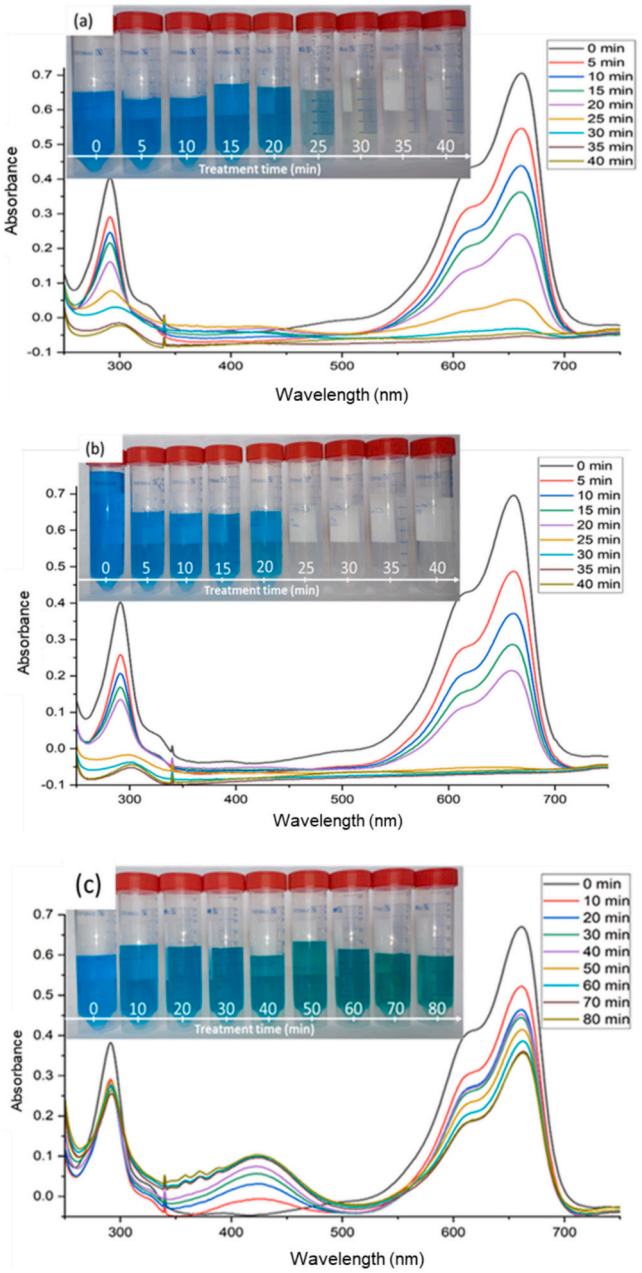


**Fig. 6.** Methylene blue degradation and variation in UV–Vis absorption spectra and the colour difference versus plasma treatment time (min) at PAW flow rate 1400 ml.min$^{-1}$ using the FDBD reactor with, (a) Cu setup, (b) Ce setup, and (c) Cuw setup. (For interpretation of the references to colour in this figure legend, the reader is referred to the web version of this article.)

pulses.

### 3.3. Dye wastewater degradation

#### 3.3.1. Effect of selective RONS production on dye degradation

Plasma-water interaction plays a crucial role in generating ROS, notably hydroxyl radicals ($OH^{\bullet}$), which are known as the primary agents for pollutant degradation in liquid. Fig. 6 shows the absorbance of methylene blue dye after plasma treatment in the FDBD reactor using the Cu and Ce setups. The absorption spectra of MB exhibit a prominent peak at 662 nm, corresponding to the MB monomer, with a shoulder peak at around 612 nm attributed to MB dimer. An additional band appears in the ultraviolet region with a peak at 292 nm, associated with substituted benzene ring [56]. These absorption peaks gradually diminish as the degradation reaction proceeds. The complete degradation of MB, without the formation of any absorbing intermediates, is characterized by the disappearance of the peaks at 662 nm or 292 nm, without the emergence of new peaks in the UV–Vis spectra. The MB dye solution becomes colourless due to the degradation of aromatic rings.

Fig. 6 also shows that the rate of reduction of the absorption peaks of MB in PAW depends on the use of different setups, with an observable effect of selective RONS production in decolorization. This observation is supported by the visible colour change in the MB solutions, which occurs significantly after 20 min of plasma treatment using the Ce setup, while with the Cu setup, the colour change gradually occurs only after 30 min of plasma treatment. This disparity can be attributed to the higher production of hydrogen peroxide by the Ce setup (Fig. 5 (a)), resulting in a faster degradation rate. The decolorization rate of the Cu setup (Fig. 6(a)), which contains ROS and RNS similar to typical DBD reactors and lacks selective ROS enhancement, results in lower degradation rates and efficiencies compared to the Ce setups with selectively enhanced ROS production (Fig. 6(b)). The efficiency of MB degradation increases with the increasing $H_2O_2$ amount. Hydrogen peroxide is known for its potent oxidizing properties, generating $O_2^{\bullet-}$ and $OH^{\bullet}$ radicals, which are primarily responsible for the degradation of MB. These reactive species ($O_2^{\bullet-}$ and $OH^{\bullet}$) initiate the redox reactions and degrade MB dye into $CO_2$, $H_2O$, or other degradation products, presumably following reactions 21–26 [57].

$$H_2O_2 + e^- \longrightarrow OH^{\bullet} + OH^- \quad (21)$$

$$H_2O_2 + h\nu \longrightarrow 2OH^{\bullet} \quad (22)$$

$$O_2 + e^- \longrightarrow O_2^{\bullet-} \quad (23)$$

$$HO_2^{\bullet} \longrightarrow H^+ + O_2^{\bullet-} \quad (24)$$

$$2O^{\bullet-} + 2H_2O \longrightarrow OH^{\bullet} + 2OH^- + O_2 \quad (25)$$

$$OH^{\bullet} + MB \longrightarrow CO_2 + H_2O + \text{Other degradation products} \quad (26)$$

Fig. 6(c) illustrates the observed colour change and absorbance of MB following plasma treatment in the FDBD reactor with the Cuw setup. The Cuw setup with higher RNS production not only shows a poor dye degradation rate but also predominantly produces other potentially hazardous by-products in wastewater treatment. This result again emphasizes the importance of tuning techniques for selective ROS production in PAW for dye degradation applications. A noticeable change from blue to green colour is observed when using the water-cooling system with higher RNS production in PAW during plasma treatment. As the treatment time progresses, the 662 nm peak diminishes, and a new peak around 424 nm appears in the UV–Vis spectra. This new peak, according to numerous references, likely signify the formation of malachite green (MG). MG typically exhibits three distinct characteristic wavelengths in UV–Vis absorption spectra, approximately at 617, 424, and 305 nm. The peak at 617 nm corresponds to chromophore of MG, while the peaks around 424 nm are attributed to the benzoic ring in the molecular structure of MG [58,59].

This phenomenon of MB conversion to MG using plasma is reported for the first time, and a further research is needed to confirm the underlying mechanism. However, it is hypothesized that the selective RNS production, generated in PAW by the Cuw setup may facilitate the nitration of MB molecular structure. A possible reaction pathway for nitration of MB during plasma treatment by Cuw setup and formation of MG is shown in Fig. 7. In this pathway, $NO_2^-$ induced in PAW facilitate the nitration of the aromatic rings in the structure of MB, resulting in the formation of nitroaromatic compounds, such as nitrobenzene. The nitration triggered by RNS is a very complex process, because the RNS formed under plasma discharge contain a wide range of nitrating agents (such as $NO_2^{\bullet}$, $HNO_2$, HOONO, and $H_2OONO^+$), which are affected by pH and the presence of organic compounds and, in turn, affect the nitration of aromatic precursors. In neutral solution, $NO_2^{\bullet}$ radical may be involved in the nitration. $NO_2^-$ plays a significant role in the formation of nitrobenzene rings, exhibiting a higher nitration rate compared to nitrate. Additionally, nitrous acid ($HNO_2$) acts as another nitrating agent, particularly active towards electron-rich compounds such as benzene rings [60].

The nitration of nitrobenzene through nitrite is intensified under acidic pH conditions after a 40 min treatment time, as observed in the Cuw setup (according to Fig. 4(b) and Fig. 6(c)). It is the reason why the increasing plasma treatment time caused a deeper green colour by the Cuw setup (Fig. 6(c)). It is worth mentioning that ROS are able to revert nitrobenzene back to benzene [61] thereby inhibiting the nitration process in PAW prepared by Ce and Cu setups which also contained $NO_2^-$ but oxidation by $H_2O_2$ dominated the MB decomposition process.

To verify the proposed nitration mechanism of MB in the Cuw plasma setup, we performed the chemical simulation of the nitration process. Nitric acid ($HNO_3$) and solid sodium nitrite ($NaNO_2$) were introduced into the MB solution as chemical agents to mimic the nitration process. The concentrations of nitric acid and $NaNO_2$ mirrored those of $NO_2^-$ and $NO_3^-$ in the Cuw plasma treatment sample at 60 min. This resulted in a pH value of 4.1 (see Fig. 4(b)), with the $NO_2^-$ concentration in the Cuw-

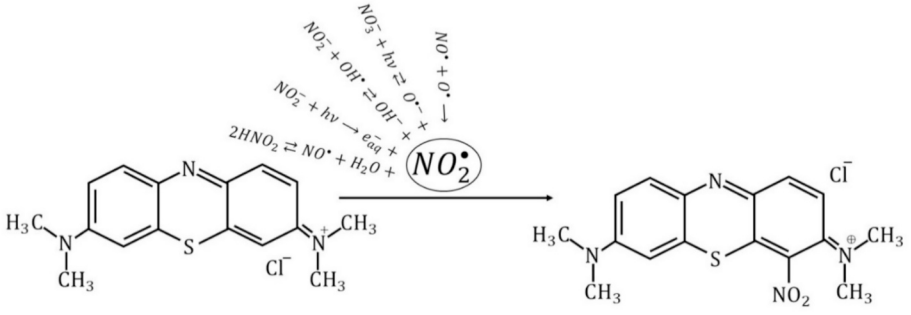


**Fig. 7.** Schematic of nitration of methylene blue by $NO_2^{\bullet}$ And formation of malachite green. (For interpretation of the references to colour in this figure legend, the reader is referred to the web version of this article.)

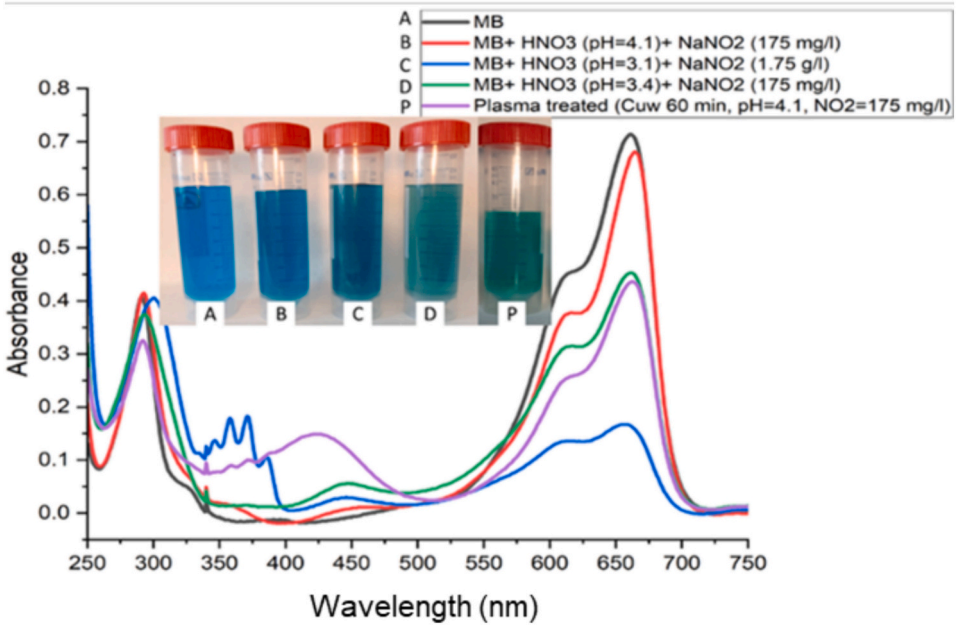


**Fig. 8.** Nitration of methylene blue, variation in UV–Vis absorption spectra and the colour difference versus chemical agents' concentrations and comparison with plasma treatment by Cuw setup. (For interpretation of the references to colour in this figure legend, the reader is referred to the web version of this article.)

treated sample after 60 min around 175 mg.l$^{-1}$ (extrapolated from Fig. 5 (c)). Intriguingly, even in the absence of plasma treatment, the introduction of nitric acid and $NaNO_2$ induced a subtle change in the colour of the MB solution after 70 h of storage. In Fig. 8, we present a comparative analysis of the UV–Vis spectra and colour change in the chemically simulated nitration of MB, showcasing the impact of varying nitric acid and $NaNO_2$ concentrations.

Notably, the absorption spectrum around 424 nm demonstrated a distinctive absorption peak formed clearly after Cuw plasma treatment, attributed to the nitration of MB molecules. However, with the same chemically added concentrations of $NO_3^-$ and $NO_2^-$ (pH = 4.1 and $NO_2^-$=175 mg.l$^{-1}$), this peak is weak. Our tests show that even with elevated levels of acidity and a tenfold increase in $NO_2^-$ concentration, the chemical reaction falls short of replicating the efficiency achieved by the plasma treatment in the Cuw setup, as illustrated in Fig. 8. This result supports the hypothesis that plasma treatment with selective RNS production (using the Cuw setup) reduces the dye degradation rate and instead modifies the molecular structures of the dye through benzoic ring nitration. This undesirable effect of plasma-driven nitration of organic molecules, from the point of view of the dye degradation, may have potential applications in chemical synthesis and especially in nitrogen fixation in organic fertilizers, making them more valuable for plant growth.

### 3.3.2. *Energy and cost efficiency*

The degradation of MB dye in water by the FDBD reactor using the Ce setup showed a higher degradation rate compared to the Cu setup, as depicted in Fig. 9(a). After 25 min of plasma treatment, the degradation rate reached up to 95 % with the Ce setup, while it was only 73 % with the Cu setup in the same time interval. It shows that the enhancement of

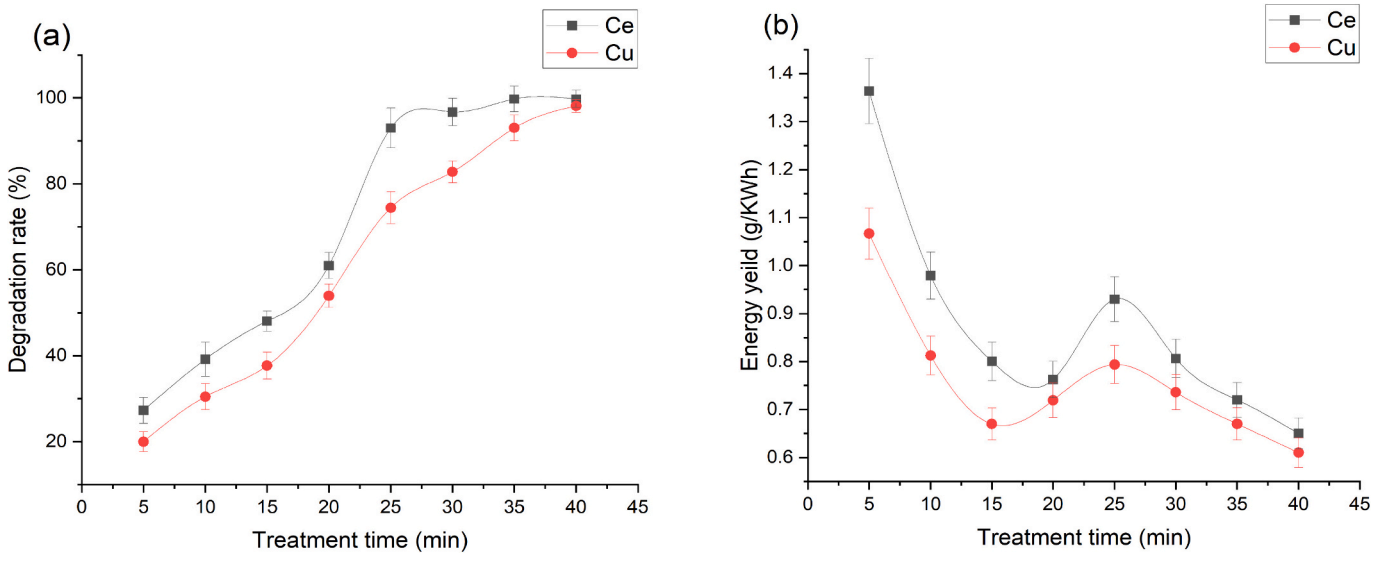


**Fig. 9.** Effect of different material as a central tube in the FDBD reactor (Initial concentration of MB = 10 mg.l$^{-1}$, water flow rate = 1400 ml.min$^{-1}$) on MB, (a) degradation constant rate, (b) and energy yield.

selective ROS production in PAW has a significant effect on the optimization of MB dye degradation by NTP. The average energy yield for MB degradation within 25 min of treatment was 1.04 g.kWh$^{-1}$ with the Ce setup and 0.83 g.kWh$^{-1}$ with the Cu setup (Fig. 9(b)). By correlating with $H_2O_2$, $NO_2^-$ and $NO_3^-$ concentrations shown in Fig. 5, we can conclude that a higher concentration of ROS in PAW can significantly increase the dye degradation rate and energy yield, while the presence of RNS in PAW leads to a lower degradation yield under the same plasma treatment time.

Non-thermal plasma-based wastewater treatment technologies rely exclusively on electricity for their operation, making them highly cost-efficient, particularly due to their low operation and maintenance (O&M) costs and the absence of chemical agent consumption. Plasma-based technologies have a wide range of wastewater treatment applications, from biologically-contaminated wastewater [32] to the degradation of hazardous persistent organic pollutants [62] and pharmaceutical compounds present in water [63]. Plasma-based water treatment integrates a comprehensive array of reactive oxidation elements that synergize with a broad spectrum of UV radiation and energetic electrons emitted during the plasma discharge process. In addition, NTP technologies offer significant advantages over currently employed AOP systems, such as $O_3$, $O_3$/UV, UV/$H_2O_2$, ultrasonic (US), and photocatalysis. However, a comprehensive economic analysis is essential for the industrial scale-up of plasma-based AOPs. Regrettably, studies that simultaneously address both the economic and technical feasibility of these plasma-based AOPs are scarce. Mahamuni and Adewuyi [64] have conducted particularly thorough review of the cost estimation of UV/US-based AOPs. Table 1 provides a comparative analysis of the cost estimates for azo-dye wastewater treatment using various AOPs technologies, with analogic data of here described FDBD plasma-based technology with Ce/Cu setup used. It underscores the significance of selective RONS production in the plasma treatment process for the cost reduction.

The total treatment costs can be represented by the sum of the capital, operating, and maintenance costs of the wastewater treatment technology. For NTP technology, the primary component of capital cost is the expenditure on plasma reactors and associated devices. Maintenance costs are primarily related to the replacement of components such as electronic circuits or power supplies. Operating costs primarily include the price of the electrical energy consumed. It should be noted that the cost of the processes depends on several factors, including the type of contaminants present, the characteristics of the wastewater, the flow rate of the effluents, and the design of the reactor. However, through a rough estimation, the total costs can be calculated based on the kinetics of the dye degradation. Applying this approach of Mahamuni and Adewuji [64], the costs have been calculated for a wastewater flow rate normalized to 1000 l.min$^{-1}$.

The time needed to reach 90 % degradation ($T_{90}$) was considered as the reference treatment time. From our MB degradation results by FDBD reactor shown in Fig. 9(a), it can be observed that using the Ce/Cu setups results in $T_{90}$ = 25/35 min, respectively. Therefore, we assume that the residence time for the proposed wastewater treatment plant using Ce/Cu setups = 25/35 min, respectively. With a design flow rate of 1000 l.min$^{-1}$ and plasma power density of 25 W.l$^{-1}$ (Fig. 2 (f)), the amount of energy needed for the plant using Ce/Cu setups ≈ 625/875 kW, respectively. This enables us to estimate the energy costs 20.84/29.18 kWh/1000 l for the FDBD Ce/Cu setups, respectively, while estimating about 50 % power losses in the power supply and dielectric tubes. This translates to the electricity cost (taking the 2010 price 0.08 $/kWh as in [64] and the conversion 1 gal = 3.785 l) of 6.4/8.8 $/1000 gal of wastewater treated for the Ce/Cu setup, respectively. These figures are comparable with or lower than the most efficient AOPs, e.g. $O_3$ (4.1 $/1000 gal), UV + $O_3$ (34 $/1000 gal) UV/$H_2O_2$ (75 $/1000 gal) or US/UV/$H_2O_2$ (65 $/1000 gal), and are much lower than other AOPs shown in Table 1 based on the review of Mahamuni and Adewuji [64].

Regarding the estimation of the reactor cost, although a low-power neon sign transformer was used in this lab-scale study, several commercial power supplies are available in market that enable scale-up and operating DBD plasma discharge with a typical power ≈ 3 kW and the price tag for one reactor based on this equipment stands at $10,000. Therefore, the number of such standard device needed for the plant will be 208/292 for Ce/Cu setups, respectively. Taking the amount of energy needed for the FDBD reactor using Ce/Cu = 625/875 kW per 1000 l.min$^{-1}$. A general estimation for capital cost can be derived by summing up the reactor cost (P), piping, valves, and electrical components (0.3P), site work (0.1P), contractor expenses (0.21P), engineering costs (0.24P), and other miscellaneous expenses (0.35P), resulting in a total of 2.2P. Therefore, the total capital cost ≈ $4.6E+06/ $6.4E+06 for Ce/Cu setup, respectively.

Annual operational cost includes electricity costs, analytical costs, labor costs, and maintenance costs.

1. Annual electrity cost: since plasma technology is solely electricity-based, electricity costs make the largest part of the O&M costs. Annual electrical costs of our FDBD reactor can be calculated by the power consumption normalized to 1000 l/min (625/875 kW for Ce/Cu setup) * time (hours per year) * price of electricity ($/kWh) ≈

**Table 1**
Cost estimation of various types of AOPs compared with nonthermal plasma-based azo-dye wastewater treatment [64].

| Method | $P^*_{elec}$ (kW) | $T^*_{90}$ (min) | V* (l) | $C_0/C^*$ (mg. l$^{-1}$) or (ppm) | Electricity cost ($/1000 gal) | Reactor cost ($/1000 gal) | Capital cost ($/1000 gal) | Annual O&M cost ($/1000 gal) | Total cost ($/1000 gal) |
|---|---|---|---|---|---|---|---|---|---|
| US (300 kHz) | 0.6 | 1316 | 1.2 | 20/2 | 14,204 | 8.23E+09 | 1.83E+10 | 5.02E+08 | 1.88E+10 |
| O3 (12.4 mg/l) | 0.636 | 208 | 1.2 | 20/2 | 4.1 | 2.04E+05 | 4.53E+05 | 1.15E+05 | 5.68E+05 |
| US + UV (254 nm) | 0.636 | 419 | 1.2 | 20/2 | 4639 | 2.64E+09 | 5.86E+09 | 1.73E+08 | 6.03E+09 |
| US + O3 (12.4 mg/L) | 0.636 | 138 | 1.2 | 20/2 | 1492 | 8.63E+08 | 1.92E+09 | 5.28E+07 | 1.97E+09 |
| UV + O3 | 0.072 | 112 | 1.2 | 20/2 | 34 | 5.04E+06 | 1.12E+07 | 3.57E+06 | 1.48E+07 |
| US/UV/O3 | 0.672 | 106 | 1.2 | 20/2 | 1187 | 6.74E+08 | 1.50E+09 | 4.43E+07 | 1.54E+09 |
| US/H2O2 | 0.066 | 60 | 4.5 | 100/46 | 416.5 | 2.40E+08 | 5.33E+08 | 1.49E+07 | 5.47E+08 |
| UV/H2O2 | 0.186 | 60 | 4.5 | 100/84 | 75 | 4.09E+07 | 9.09E+07 | 3.05E+06 | 9.39E+07 |
| US/UV/H2O2 | 0.186 | 60 | 4.5 | 100/9 | 65 | 3.60E+07 | 7.99E+07 | 2.62E+06 | 8.25E+07 |
| Photocatalysis | 0.5 | 111 | 0.7 | 402/40 | 740 | 1.20E+08 | 2.67E+08 | 8.14E+07 | 3.48E+08 |
| US + photocatalysis | 0.53 | 30 | 0.7 | 402/40 | 234 | 4.98E+07 | 1.11E+08 | 2.36E+07 | 1.35E+08 |
| NTP FDBD Cu, without selective RONS production (this work) | 0.025 | 35 | 1 | 10/1 | 8.8 | 2.92E+06 | 6.42E+06 | 1.0E+06 | 7.42E+06 |
| NTP FDBD Ce, with selective RONS production (this work) | 0.025 | 25 | 1 | 10/1 | 6.4 | 2.08E+06 | 4.58E+06 | 7.28E+05 | 5.30E+06 |

* Electric power ($P_{elec}$), treatment time needed to reach 90 % degradation ($T_{90}$), tested water volume (V), initial ($C_0$) and final (C) pollutant concentration.

$4.4E+05/$6.2E+05 for Ce/Cu setup, respectively (assuming $0.08/kWh to be comparable with AOPs reviewed by [64]).
2. Analytical cost: annual analysis labor*analysis cost = 4 (h/week)* 52 (week) * 200 $/h ≈ $4.2E+04
3. Labor cost: annual sampling labor* labor cost = 4 (h/week)* 52 (week)* 80 $/h ≈ $1.7E+04,
4. Maintenance cost is mostly due to the part replacement cost and is assumed≈ 5 % capital cost.

Taken together, the annual O&M costs of the FDBD reactor are as low as 7.28E+05/1.0E+06 $ for Ce/Cu setup, respectively. Also accounting for the capital costs, the total costs of our potentially scaled-up FDBD reactor would be $5.3E+06/$7.4E+06 for Ce/Cu setup, respectively, which belongs among the least expensive AOPs. Especially the low O&M costs allow us to generalize that NTP technology offers significant advantages over currently employed AOPs that stem from their ability to form and incorporate nearly all reactive oxidation species in a greater extent than AOPs, furthermore in synergy with both UV radiation and energetic electrons and ions emitted from the plasma discharge.

Once again, it is evident that the proposed approach of selective RONS production with optimized ROS for the dye degradation using the NTP technology by the FDBD reactor with ceramic electrode, leads to a significant reduction in total costs, estimated to be close to 30 %. This study emphasizes the critical importance of fine tuning the system for selective ROS production in water, not only for practical efficacy but also for economic efficiency. Without proper tuning, the potential production of RNS in wastewater treatment can result in hazardous nitrated aromatic by-products or significantly reduce the process efficiency. To address this challenge, we advocate for the implementation of implicit techniques for tuning RONS in PAW. This strategy will ensure that plasma-based wastewater treatment remains effective, safe, and environmentally sustainable in various scenarios. Future research efforts could explore the applicability of our tuning technique to further enhance the capabilities of PAW applications.

## 4. Conclusion

The fountain dielectric barrier discharge (FDBD) reactor designed as a coaxial cylindrical system with a variable central electrode and a water-cooling system, enables water to cascade down in a thin film layer from the top of the central tube, effectively using water as the central electrode. This innovative setup allows for the substitution of the central tube with a nonconductive material, enabling us the flexibility to control ROS and RNS production in the generated plasma-activated water (PAW). We investigated two different materials as the central tube in the FDBD reactor: copper (Cu) and alumina ceramic (Ce). Additionally, we demonstrated the significant influence of the reactor temperature on RONS production in PAW by utilizing a water-cooling system with different central tube materials (Cuw and Cew).

The PAW generated by the various setups (Cu, Ce, Cuw, and Cew) in the FDBD reactor exhibited variations in the produced concentrations of hydrogen peroxide ($H_2O_2$), nitrite ($NO_2^-$), and nitrate ($NO_3^-$). Notably, the Cu setup displayed a non-linear rise and fall trend in $H_2O_2$ concentration, while the Ce setup exhibited its linear increase, resulting in significantly higher $H_2O_2$ concentration in PAW. On the other hand, the Cuw and Cew setups did not produce $H_2O_2$, but instead showed notably higher concentrations of $NO_2^-$ ions compared to the Cu and Ce setups.

Furthermore, our research underscores the critical importance of tuning the ROS and RNS components in PAW for dye degradation applications. We demonstrated that the FDBD setup for increasing ROS production can enhance energy efficiency more than 20 % compared to a typical DBD reactor producing a mixture of ROS and RNS. UV–vis analysis of water contaminated with a model textile azo dye methylene blue (MB) treated using different setups in the FDBD reactor revealed dominant degradation processes. The Ce setup, producing higher levels of ROS, especially $H_2O_2$, displayed a more pronounced degradation and stronger discoloration efficiency of MB, both in terms of energy yield and degradation rate. Conversely, the dominant presence of RNS in the treatment process by the Cuw setup, which led to the nitration of MB molecular structure, not only decreased the efficiency of MB degradation but also generated potentially hazardous by-product components.

These findings highlight the necessity of precise control over ROS and RNS production in PAW for effective dye degradation applications and underscore the potential of tuning techniques to enhance the water treatment efficiency while minimizing hazardous by-products. Moreover, the total cost estimation for plasma-based water treatment compared with other AOPs shows that plasma technology potentially offers one of the lowest total costs. It also suggests that the system tuning with selective RONS production for the dye degradation can lead to a substantial almost 30 % reduction in total costs. This approach guarantees the effectiveness, safety, and environmental sustainability of plasma-based wastewater treatment in different scenarios. Future research efforts could investigate the potential application of our tuning technique to further improve PAW applications.

## CRediT authorship contribution statement

**Saeed Kooshki:** Writing – review & editing, Writing – original draft, Visualization, Validation, Methodology, Investigation, Formal analysis, Data curation, Conceptualization. **Pankaj Pareek:** Writing – review & editing, Validation, Investigation. **Mario Janda:** Writing – review & editing, Validation, Resources, Investigation, Formal analysis. **Zdenko Machala:** Writing – review & editing, Validation, Supervision, Resources, Investigation, Funding acquisition, Formal analysis.

## Declaration of competing interest

N/A.

## Data availability

The data that has been used is confidential.

## Acknowledgment

This work was supported by Slovak Research and Development Agency grants APVV-22-0247, APVV-20-0566, and APVV-17-0382, Slovak Grant Agency VEGA 1/0596/22, and by COST Action CA19110 “PlAgri” (supported by European Cooperation in Science and Technology).

## References

[1] R. Thirumdas, et al., Plasma activated water (PAW): chemistry, physico-chemical properties, applications in food and agriculture, Trends Food Sci. Technol. 77 (2018) 21–31, https://doi.org/10.1016/j.tifs.2018.05.007.
[2] K. Tachibana, T. Nakamura, Comparative study of discharge schemes for production rates and ratios of reactive oxygen and nitrogen species in plasma activated water, J. Phys. Appl. Phys. 52 (38) (2019) 385202, https://doi.org/10.1088/1361-6463/ab2529.
[3] R. Zhou, et al., Plasma-activated water: generation, origin of reactive species and biological applications, J. Phys. Appl. Phys. 53 (30) (2020) 303001, https://doi.org/10.1088/1361-6463/ab81cf.
[4] P.G. Subramanian, A. Jain, A.M. Shivapuji, N.R. Sundaresan, S. Dasappa, L. Rao, Plasma-activated water from a dielectric barrier discharge plasma source for the selective treatment of cancer cells, Plasma Processes Polym. 17 (8) (2020) 1900260, https://doi.org/10.1002/ppap.201900260.
[5] P. Lukes, E. Dolezalova, I. Sisrova, M. Clupek, Aqueous-phase chemistry and bactericidal effects from an air discharge plasma in contact with water: evidence for the formation of peroxynitrite through a pseudo-second-order post-discharge reaction of H2O2 and HNO2, Plasma Sources Sci. Technol. 23 (1) (2014) 015019, https://doi.org/10.1088/0963-0252/23/1/015019.
[6] N. Rao, et al., Algal cell inactivation and damage via cold plasma-activated bubbles: mechanistic insights and process benefits, Chem. Eng. J. 454 (2023) 140304, https://doi.org/10.1016/j.cej.2022.140304.
[7] A. Soni, J. Choi, G. Brightwell, Plasma-activated water (PAW) as a disinfection technology for bacterial inactivation with a focus on fruit and vegetables, Foods 10 (1) (2021) 166, https://doi.org/10.3390/foods10010166.

[8] I.-E. Vlad, S.D. Anghel, Time stability of water activated by different on-liquid atmospheric pressure plasmas, J. Electrostat. 87 (2017) 284–292, https://doi.org/10.1016/j.elstat.2017.06.002.

[9] R. Zhou, et al., Cold atmospheric plasma activated water as a prospective disinfectant: the crucial role of peroxynitrite, Green Chem. 20 (23) (2018) 5276–5284, https://doi.org/10.1039/C8GC02800A.

[10] N. Punith, R. Harsha, R. Lakshminarayana, M. Hemanth, M.S. Anand, S. Dasappa, Plasma activated water generation and its application in agriculture, Adv. Mater. Lett. 10 (10) (2019) 700–704, https://doi.org/10.5185/amlett.2019.0042.

[11] B. Šerá, V. Scholtz, J. Jirešová, J. Khun, J. Julák, M. Šerý, Effects of non-thermal plasma treatment on seed germination and early growth of leguminous plants—a review, Plants 10 (8) (2021) 1616, https://doi.org/10.3390/plants10081616.

[12] P. Bruggeman, C. Leys, Non-thermal plasmas in and in contact with liquids, J. Phys. Appl. Phys. 42 (5) (2009) 053001, https://doi.org/10.1088/0022-3727/42/5/053001.

[13] G.J. Lee, et al., Nitrate capture investigation in plasma-activated water and its antifungal effect on Cryptococcus pseudolongus cells, Int. J. Mol. Sci. 22 (23) (2021) 12773, https://doi.org/10.3390/ijms222312773.

[14] P. Lamichhane, B. Ghimire, S. Mumtaz, R. Paneru, S.H. Ki, E.H. Choi, Control of hydrogen peroxide production in plasma activated water by utilizing nitrification, J. Phys. Appl. Phys. 52 (26) (2019) 265206, https://doi.org/10.1088/1361-6463/ab16a9.

[15] X. Gao, K. Huang, A. Zhang, C. Wang, Z. Sun, Y. Liu, Simultaneous degradation of glucocorticoids and sterilization using bubbling corona discharge plasma based systems: a promising terminal water treatment facility for hospital wastewater, Chem. Eng. J. 430 (2022) 132845, https://doi.org/10.1016/j.cej.2021.132845.

[16] B. Jiang, et al., Review on electrical discharge plasma technology for wastewater remediation, Chem. Eng. J. 236 (2014) 348–368, https://doi.org/10.1016/j.cej.2013.09.090.

[17] H. Xu, C. Liu, Q. Huang, Enhance the inactivation of fungi by the sequential use of cold atmospheric plasma and plasma-activated water: synergistic effect and mechanism study, Chem. Eng. J. 452 (2023) 139596, https://doi.org/10.1016/j.cej.2022.139596.

[18] P. Lamichhane, et al., Non-thermal argon plasma jets of various lengths for selective reactive oxygen and nitrogen species production, J. Environ. Chem. Eng. 10 (3) (2022) 107782, https://doi.org/10.1016/j.jece.2022.107782.

[19] S. Reuter, et al., From RONS to ROS: tailoring plasma jet treatment of skin cells, IEEE Trans. Plasma Sci. 40 (11) (2012) 2986–2993, https://doi.org/10.1109/TPS.2012.2207130.

[20] T. Ito, G. Uchida, A. Nakajima, K. Takenaka, Y. Setsuhara, Control of reactive oxygen and nitrogen species production in liquid by nonthermal plasma jet with controlled surrounding gas, Jpn. J. Appl. Phys. 56 (1S) (2016) 01AC06, https://doi.org/10.7567/JJAP.56.01AC06.

[21] R. Hawtof, S. Ghosh, E. Guarr, C. Xu, R. Mohan Sankaran, J.N. Renner, Catalyst-free, highly selective synthesis of ammonia from nitrogen and water by a plasma electrolytic system, Sci. Adv. 5 (1) (2019) eaat5778, https://doi.org/10.1126/sciadv.aat5778.

[22] Z. Machala, B. Tarabová, D. Sersenová, M. Janda, K. Hensel, Chemical and antibacterial effects of plasma activated water: correlation with gaseous and aqueous reactive oxygen and nitrogen species, plasma sources and air flow conditions, J. Phys. Appl. Phys. 52 (3) (2018) 034002, https://doi.org/10.1088/1361-6463/aae807.

[23] K. Hensel *et al.*, 'Effects of air transient spark discharge and helium plasma jet on water, bacteria, cells, and biomolecules', Biointerphases, vol. 10, no. 2, p. 029515, 2015. dx.doi:https://doi.org/10.1116/1.4919559.

[24] G. Uchida, et al., Effects of nonthermal plasma jet irradiation on the selective production of H2O2 and NO2− in liquid water, J. Appl. Phys. 120 (20) (2016) 203302, https://doi.org/10.1063/1.4968568.

[25] V. Rathore, S.K. Nema, Selective generation of reactive oxygen species in plasma-activated water using CO2 plasma, J. Vac. Sci. Technol. A 41 (4) (2023), https://doi.org/10.1116/6.0002460.

[26] P. Lu, D. Boehm, P. Bourke, P.J. Cullen, Achieving reactive species specificity within plasma-activated water through selective generation using air spark and glow discharges, Plasma Processes Polym. 14 (8) (2017) 1600207, https://doi.org/10.1002/ppap.201600207.

[27] W.-H. Hsu, et al., Femtosecond laser-induced hard X-ray generation in air from a solution flow of au nano-sphere suspension using an automatic positioning system, Opt. Express 24 (18) (2016) 19994–20001, https://doi.org/10.1364/OE.24.019994.

[28] M. Schneider, R. Rataj, L. Bláha, J.F. Kolb, Experimental review of different plasma technologies for the degradation of cylindrospermopsin as model water pollutant, Chem. Eng. J. 451 (2023) 138984, https://doi.org/10.1016/j.cej.2022.138984.

[29] Y.S. Jin, C. Cho, D. Kim, C.H. Sohn, C. Ha, S.-T. Han, Mass production of plasma activated water by an atmospheric pressure plasma, Jpn. J. Appl. Phys. 59 (SH) (2020) SHHF05, https://doi.org/10.35848/1347-4065/ab7e13.

[30] P. Subramanian, H. Rao, A.M. Shivapuji, P.-L. Girard-Lauriault, L. Rao, Plasma-activated water from DBD as a source of nitrogen for agriculture: Specific energy and stability studies, J. Appl. Phys. 129 (9) (2021), https://doi.org/10.1063/5.0039253.

[31] S. Pandey, et al., Selective generation of nitrate and nitrite in plasma activated water and its physicochemical parameters analysis, Phys. Lett. A 474 (2023) 128832, https://doi.org/10.1016/j.physleta.2023.128832.

[32] S. Kooshki, P. Pareek, R. Mentheour, M. Janda, Z. Machala, Efficient treatment of bio-contaminated wastewater using plasma technology for its reuse in sustainable agriculture, Environ. Technol. Innov. (2023) 103287, https://doi.org/10.1016/j.eti.2023.103287.

[33] V.V. Kovačević, B.P. Dojčinović, M. Jović, G.M. Roglić, B.M. Obradović, M. M. Kuraica, Measurement of reactive species generated by dielectric barrier discharge in direct contact with water in different atmospheres, J. Phys. Appl. Phys. 50 (15) (2017) 155205, https://doi.org/10.1088/1361-6463/aa5fde.

[34] B. Wang, B. Dong, M. Xu, C. Chi, C. Wang, Degradation of methylene blue using double-chamber dielectric barrier discharge reactor under different carrier gases, Chem. Eng. Sci. 168 (2017) 90–100, https://doi.org/10.1016/j.ces.2017.04.027.

[35] G. Eisenberg, Industrial and engineering chemistry, Ind. Eng. Chem. Anal. Ed. 15 (1943) 327–328.

[36] A. Ozkan, et al., DBD in burst mode: solution for more efficient CO2 conversion? Plasma Sources Sci. Technol. 25 (5) (2016) 055005, https://doi.org/10.1088/0963-0252/25/5/055005.

[37] V. Rathore, S.K. Nema, A comparative study of dielectric barrier discharge plasma device and plasma jet to generate plasma activated water and post-discharge trapping of reactive species, Phys. Plasmas 29 (3) (2022) 033510, https://doi.org/10.1063/5.0078823.

[38] J.-P. Liang, et al., Comparison of gas phase discharge and gas-liquid discharge for water activation and methylene blue degradation, Vacuum 181 (2020) 109644, https://doi.org/10.1016/j.vacuum.2020.109644.

[39] D. Popović, V. Milosavljević, S. Daniels, Practical sensor for nitrogen in direct current glow discharges, J. Appl. Phys. 102 (10) (2007) 103303, https://doi.org/10.1063/1.2816254.

[40] Z. Fan, H. Yan, Y. Wang, Y. Liu, H. Guo, C. Ren, Breakdown characteristics of atmospheric dielectric barrier discharge in gas flow condition, Phys. Plasmas 25 (5) (2018) 053517, https://doi.org/10.1063/1.5018331.

[41] C. Laux, Radiation and Nonequilibrium Collisional-Radiative Models, von Karman Institute Lecture Series 2002–07 Rhode-Saint-Genèse, 2002.

[42] G. Duarte, Characterization of a Novel Double Cooled Electrode DBD Reactor for Ozone Generation. https://scholarship.shu.edu/dissertations/2808, 2020.

[43] R. Mandal, A. Singh, A.P. Singh, Recent developments in cold plasma decontamination technology in the food industry, Trends Food Sci. Technol. 80 (2018) 93–103, https://doi.org/10.1016/j.tifs.2018.07.014.

[44] Y. Gorbanev, D. O'Connell, V. Chechik, Non-thermal plasma in contact with water: the origin of species, Chem. A Eur. J. 22 (10) (2016) 3496–3505, https://doi.org/10.1002/chem.201503771.

[45] S. Xu, V. Jirasek, P. Lukes, Molecular dynamics simulations of singlet oxygen atoms reactions with water leading to hydrogen peroxide, J. Phys. Appl. Phys. 53 (27) (2020) 275204, https://doi.org/10.1088/1361-6463/ab8321.

[46] S. Kanazawa, et al., Observation of OH radicals produced by pulsed discharges on the surface of a liquid, Plasma Sources Sci. Technol. 20 (3) (2011) 034010, https://doi.org/10.1088/0963-0252/20/3/034010.

[47] P. Bruggeman, D.C. Schram, On OH production in water containing atmospheric pressure plasmas, Plasma Sources Sci. Technol. 19 (4) (2010), https://doi.org/10.1088/0963-0252/19/4/045025.

[48] J. Chauvin, F. Judée, M. Yousfi, P. Vicendo, N. Merbahi, Analysis of reactive oxygen and nitrogen species generated in three liquid media by low temperature helium plasma jet, Sci. Rep. 7 (1) (2017) 1–15, https://doi.org/10.1038/s41598-017-04650-4.

[49] V. Rathore, C. Patil, A. Sanghariyat, S.K. Nema, Design and development of dielectric barrier discharge setup to form plasma-activated water and optimization of process parameters, Eur. Phys. J. D 76 (5) (2022) 77, https://doi.org/10.1140/epjd/s10053-022-00397-4.

[50] K. Kutasi, N. Krstulović, A. Jurov, K. Salamon, D. Popović, S. Milošević, Controlling: the composition of plasma-activated water by cu ions, Plasma Sources Sci. Technol. 30 (4) (2021) 045015, https://doi.org/10.1088/1361-6595/abf078.

[51] B. Wagner, S. Garboś, E. Bulska, A. Hulanicki, Determination of iron and copper in old manuscripts by slurry sampling graphite furnace atomic absorption spectrometry and laser ablation inductively coupled plasma mass spectrometry, Spectrochim. Acta Part B At. Spectrosc. 54 (5) (1999) 797–804, https://doi.org/10.1016/S0584-8547(99)00025-7.

[52] E. Corella Puertas, A. Dzafic, S. Coulombe, Investigation of the electrode erosion in pin-to-liquid discharges and its influence on reactive oxygen and nitrogen species in plasma-activated water, Plasma Chem. Plasma Process. 40 (2020) 145–167, https://doi.org/10.1007/s11090-019-10036-3.

[53] A.N. Pham, G. Xing, C.J. Miller, T.D. Waite, Fenton-like copper redox chemistry revisited: hydrogen peroxide and superoxide mediation of copper-catalyzed oxidant production, J. Catal. 301 (2013) 54–64, https://doi.org/10.1016/j.jcat.2013.01.025.

[54] S.A. Center, K.P. Richter, D.C. Twedt, J.J. Wakshlag, P.J. Watson, C.R. Webster, Is it time to reconsider current guidelines for copper content in commercial dog foods? J. Am. Vet. Med. Assoc. 258 (4) (2021) 357–364, https://doi.org/10.2460/javma.258.4.357.

[55] C. Bradu, K. Kutasi, M. Magureanu, N. Puač, S. Živković, Reactive nitrogen species in plasma-activated water: generation, chemistry and application in agriculture, J. Phys. Appl. Phys. 53 (22) (2020) 223001, https://doi.org/10.1088/1361-6463/ab795a.

[56] I. Khan, et al., Review on methylene blue: its properties, uses, toxicity and photodegradation, Water 14 (2) (2022) 242, https://doi.org/10.3390/w14020242.

[57] X. Zhang, et al., Research on methylene blue degradation based on multineedle-to-plane liquid dielectric barrier discharge mode, Sep. Purif. Technol. 286 (2022) 120476, https://doi.org/10.1016/j.seppur.2022.120476.

[58] H. Bel Hadjltaief, A. Omri, M. Ben Zina, P. Da Costa, M.E. Galvez, Titanium dioxide supported on different porous materials as photocatalyst for the degradation of methyl green in wastewaters, Adv. Mater. Sci. Eng. 2015 (2015), https://doi.org/10.1155/2015/759853.

[59] V. Chaturvedi, P. Verma, Biodegradation of malachite green by a novel copper-tolerant Ochrobactrum pseudogrignonense strain GGUPV1 isolated from copper mine waste water, Bioresour. Bioprocess. 42 (2015), https://doi.org/10.1186/s40643-015-0070-8.
[60] G. Marussi, D. Vione, Secondary formation of aromatic nitroderivatives of environmental concern: Photonitration processes triggered by the photolysis of nitrate and nitrite ions in aqueous solution, Molecules 26 (9) (2021) 2550, https://doi.org/10.3390/molecules26092550.
[61] M. Hayyan, M.A. Hashim, I.M. AlNashef, Superoxide ion: generation and chemical implications, Chem. Rev. 116 (5) (2016) 3029–3085, https://doi.org/10.1021/acs.chemrev.5b00407.
[62] N. Takeuchi, K. Yasuoka, Review of plasma-based water treatment technologies for the decomposition of persistent organic compounds, Jpn. J. Appl. Phys. 60 (2021) 0801–0813, https://doi.org/10.35848/1347-4065/abb75d.
[63] M. Magureanu, N.B. Mandache, V.I. Parvulescu, Degradation of pharmaceutical compounds in water by non-thermal plasma treatment, Water Res. 81 (2015) 124–136, https://doi.org/10.1016/j.watres.2015.05.037.
[64] N.N. Mahamuni, Y.G. Adewuyi, Advanced oxidation processes (AOPs) involving ultrasound for waste water treatment: a review with emphasis on cost estimation, Ultrason. Sonochem. 17 (2010) 990–1003, https://doi.org/10.1016/j.ultsonch.2009.09.005.